

High resolution atmospheric inversion of urban CO₂ emissions during the dormant season of the Indianapolis Flux Experiment (INFLUX)

Thomas Lauvaux^{1,2}, Natasha L. Miles¹, Aijun Deng¹, Scott J. Richardson¹, Maria O. Cambaliza^{7,8}, Kenneth J. Davis¹, Brian Gaudet¹, Kevin R. Gurney³, Jianhua Huang³, Darragh O’Keefe³, Yang Song³, Anna Karion⁹, Tomohiro Oda^{4,5}, Risa Patarasuk³, Igor Razlivanov³, Daniel Sarmiento¹, Paul Shepson⁶, Colm Sweeney⁹, Jocelyn Turnbull^{9,10}, and Kai Wu¹

¹The Pennsylvania State University, Department of Meteorology, University Park

²NASA Jet Propulsion Laboratory, Pasadena, CA

³Arizona State University, Phoenix, AZ

⁴Global Modeling and Assimilation Office, NASA Goddard Space Flight Center, Greenbelt, MD

⁵Goddard Earth Sciences Technologies and Research, Universities Space Research Association, Columbia, MD

⁶Purdue University, West Lafayette, IN

⁷Ateneo de Manila University, Department of Physics, Quezon City, Philippines

⁸Ateneo de Manila Campus, Manila Observatory, Quezon City, Philippines

⁹University of Colorado, CIRES, Boulder, CO

¹⁰NOAA Earth System Research Laboratory, Boulder, Colorado

¹¹National Isotope Centre, GNS Science, Lower Hutt, New Zealand

Correspondence to: Thomas Lauvaux (tul5@psu.edu)

Abstract. Urban emissions of greenhouse gases (GHG) represent more than 70% of the global fos-

sil fuel GHG emissions. Unless mitigation strategies are successfully implemented, the increase in urban GHG emissions is almost inevitable as large metropolitan areas are projected to grow twice as fast as the world population in the coming 15 years. Monitoring these emissions becomes a critical

5 need as their contribution to the global carbon budget increases rapidly. In this study, we developed the first comprehensive monitoring systems of CO₂ emissions at high resolution using a dense network of CO₂ atmospheric measurements over the city of Indianapolis. The inversion system was evaluated over a 8-month period and showed an increase compared to the Hestia CO₂ emission estimate, a state-of-the-art building-level emission product, with a 20% increase in the total emissions

10 over the area (from 4.5 to 5.7 MtC \pm 0.23 MtC). However, several key parameters of the inverse system need to be addressed to carefully characterize the spatial distribution of the emissions and the aggregated total emissions. We found that spatial structures in prior emission errors, mostly undetermined, affect significantly the spatial pattern in the inverse solution, as well as the carbon budget over the urban area. Several other parameters of the inversion were sufficiently constrained by additional
15 observations such as the characterization of the GHG boundary inflow and the introduction of hourly transport model errors estimated from the meteorological assimilation system. Finally, we estimated the uncertainties associated with remaining systematic errors and undetermined parameters using

an ensemble of inversions. The total CO₂ emissions for the Indianapolis urban area based on the ensemble mean and quartiles are 5.26 - 5.91 MtC, *i.e.* a statistically significant difference compared to the prior total emissions of 4.1 to 4.5 MtC. We therefore conclude that atmospheric inversions are potentially able to constrain the carbon budget of the city, assuming sufficient data to measure the inflow of GHG over the city, but additional information on prior emissions and their associated error structures are required if we are to determine the spatial structures of urban emissions at high resolution.

1 Introduction

The increase in the atmospheric concentration of carbon dioxide (CO₂) reached the fastest decadal rate over the period 2002-2011 with 2 ± 0.1 ppm/yr. Consequently, CO₂ remains the largest single contributor to the increase in the anthropogenic radiative forcing (IPCC, 2014), with 80% of the emissions originating from fossil fuel combustion and industrial processes. Quantification of anthropogenic CO₂ emissions is typically accomplished via bottom-up accounting or inventory methods at global (e.g. Marland et al. (1985); Andres et al. (1996, 2012); Asefi-Najafabady et al. (2014)) and regional scales (Gurney et al., 2009, 2012). These inventories remain affected by large uncertainties (Andres et al., 2014) which increases at higher spatial and temporal resolutions (*e.g.* Turnbull et al. (2011)). As legislation to regulate GHG emissions becomes increasingly likely, independent verification of inventory-based anthropogenic emissions becomes an emerging need (NRC, 2010).

Urban CO₂ emissions represent about 70% of the global emissions and will likely increase as large metropolitan areas are projected to grow twice as fast as the world population in the coming 15 years (United Nations and Social Affairs, 2014). Monitoring urban emissions using independent approaches is therefore a critical need for current and future regulation policies with atmospheric inversion techniques being a potential candidate to provide a robust and complementary approach to current reporting activities (Nisbet and Weiss, 2010). However, a better understanding of the underlying human activities remains critical for policy decisions and mitigation strategies (Hutyra et al., 2014), which implies the use of process-oriented systems, highly resolved in both space and time (Gurney et al., 2012). Current atmospheric inversion systems remain too coarse spatially and are limited to constraining the emissions rather than the underlying processes (). Therefore, higher resolution inverse systems are needed to better understand and quantify the emissions by sector (e.g. manufacturing sources, power generation sources, mobile sources) in support of future policies.

This lack of well-established methods for quantifying spatially and temporally resolved GHG emissions applies to urban areas. Recent studies have provided high-resolution emission products separated by sector (Gurney et al., 2012), but are difficult to assemble and very likely prone to systematic errors (Gurney, 2014). Atmospheric methods offer a unique angle on urban emissions by capturing the accumulated atmospheric signals emitted from all sectors of activity (Turnbull et al.,

2011). But these methods are also limited by various sources of errors, mostly due to the atmospheric transport models (Gerbig et al., 2003; Diaz-Isaac et al., 2014) and the incorrect characterization of prior flux errors (Koohkan and Bocquet, 2012), as well as by the amount of atmospheric measurements available over the region of interests. At moderate resolutions (10-40km), atmospheric inversions using regional atmospheric transport models (Lauvaux et al., 2012; Schuh et al., 2013) have the potential to provide spatially and temporally resolved GHG surface fluxes (Ogle et al., 2015). At higher resolutions, several studies have shown the potential of atmospheric systems to detect emissions (McKain et al., 2012; Kort et al., 2012; Bréon et al., 2015) but this approach has not yet been fully implemented over small domains with the high resolution required for urban areas.

The inversion of large point sources and well-defined emitting areas are particularly sensitive to the transport model and the representation of plume structures over flat or complex terrain, especially for observations within the urban domain (Bréon et al., 2015). Large spatial and temporal gradients in urban emissions generate large gradients in atmospheric mixing ratios. Therefore, the development of accurate atmospheric modeling systems able to simulate these gradients is a prerequisite to the detection and quantification of emissions over highly contrasted urban environment. High-density observations combined with high-resolution atmospheric modeling has the potential to yield such resolution over small domains. At the mechanistic level, processes from specific sectors of the economy shape the spatial pattern of GHG emissions across urban centers. But atmospheric inversions have not yet been used to separate the contributions from individual sectors of the economy (Djuricin et al., 2012) or to separate biogenic and anthropogenic sources (Djuricin et al., 2010). Expanding the atmospheric inversion systems to include trace gas measurements, including isotopic tracers, offers the capability to measure the fraction of the signals related to fossil fuel consumption (Turnbull et al., 2015) and perhaps sectoral emissions. In this context, the Indianapolis Flux Experiment (INFLUX) is exploring the technical limits of this method for inferring highly resolved anthropogenic GHG emissions estimates.

Here, we present the first atmospheric inversion system producing high-resolution GHG emissions of CO₂ at the urban scale, assimilating both atmospheric mixing ratios of greenhouse gases and meteorological measurements. The inverse modeling system is able to derive spatially and temporally resolved urban CO₂ emissions within a large urban area, starting with a high resolution emission product, Hestia (Gurney et al., 2012). First, we developed an atmospheric Four-Dimensional Data Assimilation (FDDA) modeling system at 1km spatial resolution assimilating continuously meteorological measurements to improve the representation of the local atmospheric dynamics. Transport errors associated with the atmospheric modeling system are then quantified as a function of the accuracy of different meteorological variables. Second, we demonstrate the current inversion system ability to monitor GHG emissions using a high-density spatially-distributed atmospheric observing network of instrumented towers, using two existing high-resolution CO₂ emissions products. Finally,

we construct an ensemble of inverse solutions to represent additional sources of errors in the current
90 inversion system and quantify the uncertainties associated with parameters in the system.

2 Methods

2.1 Atmospheric modeling system

2.1.1 Atmospheric Four Dimensional Data Assimilation (FDDA) modeling system

The core of our realtime modeling system Deng et al. (2012a) used in this research is the Weather
95 Research and Forecasting model coupled with Chemistry (WRF-Chem, Grell et al. (2005)) modified
for passive tracers as in Lauvaux et al. (2012). The WRF configuration for the model physics used
here was based on previous numerical modeling studies (e.g., Gaudet et al. (2009); Rogers et al.
(2013); Deng et al. (2012b)) using: 1) the single-Moment 3-class simple ice scheme for microphys-
ical processes, 2) the Kain-Fritsch scheme for cumulus parameterization on the 9-km grid, 3) the
100 Rapid Radiative Transfer Model for longwave atmospheric radiation, and the Dudhia scheme for
shortwave atmospheric radiation, 4) the Turbulent Kinetic Energy (TKE)-predicting Mellor-Yamada-
Jancic (MYJ) Level 2.5 turbulent closure scheme for the turbulence parameterization in the Planetary
Boundary Layer (PBL), and 5) the 5-layer thermal diffusion scheme for representation of the inter-
action between the land surface and the atmospheric surface layer (Skamarock et al., 2008).

105 The WRF modeling system used in this study has FDDA capabilities to allow the meteoro-
logical observations to be continuously assimilated into the model. The FDDA technique used
in this study was originally developed for MM5 (Stauffer and Seaman, 1994) and recently imple-
mented into WRF (Deng et al., 2009) and has been used in several studies (e.g., Rogers et al. (2013);
Lauvaux et al. (2013)). Nudging of the wind field is applied through all model layers, but nudging
110 of the mass fields (temperature and moisture) is only allowed above the model-simulated PBL so
that the PBL structure produced by the model is dominated by the model physics. In this specific
application, the World Meteorological Organization (WMO) observations were assimilated into the
WRF-Chem system to produce a dynamic analysis, blending the model simulations and the obser-
vations to produce the most accurate meteorological conditions possible to simulate the atmospheric
115 CO₂ concentrations in space and time throughout the Indianapolis region.

The WRF model grid configuration used for this demonstration is comprised of three grids: 9-km,
3-km and 1-km (cf. Fig. 1 for the 3-km and 1-km grids), all of which are co-centered at Indianapolis,
Indiana. The 9-km grid, with a mesh of 100x100 grid points, contains the eastern part of the US
Midwest. The 3-km grid, with a mesh of 99x99 grid points, contains the southern part of the state of
120 Indiana. The 1-km grid, with a mesh of 87x87, covers the metropolitan area of Indianapolis and the
8 eight counties surrounding Marion county. 59 vertical terrain-following layers are used, with the

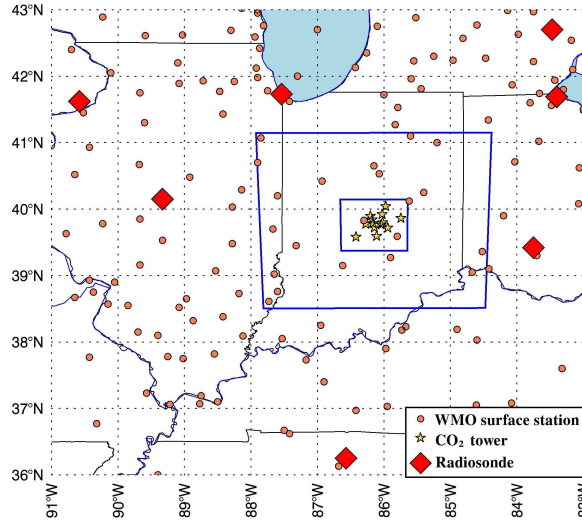


Figure 1. Surface meteorological observation distribution including surface meteorological stations (red circles) and rawinsondes (red diamonds) from the WMO database used in the WRF-FDDA modeling system, and CO₂ tower locations (gold star) in the 1km simulation domain (blue square). Indianapolis is located at the center of the domains.

center point of the lowest model layer located ~ 6 m above ground level (AGL). The thickness of the layers increases gradually with height, with 25 layers below 850 hPa (~ 1550 m AGL).

The FDDA parameters used in this application can be found in Deng et al. (2012a). For this application, 3D analysis nudging and surface analysis nudging were applied on the 9-km grid with reduced nudging strength compared to observation nudging, and observation nudging was applied on all grids with the same nudging strength. No mass fields (temperature and moisture) observations are assimilated within the WRF-predicted PBL. The meteorological observations assimilated into the WRF system are based on the WMO observations distributed by the National Weather Service (NWS), and include both 12-hourly upper-air rawinsondes and hourly surface observations. Figure 1 shows the WMO surface observation distributions, indicating a significant amount of observations over the region. The gridded meteorological data used to initialize the WRF-Chem realtime system was the National Centers for Environmental Prediction (NCEP) North American Regional Reanalysis (NARR) available every 3 hours.

2.2 Lagrangian Particle Dispersion Modeling

The Lagrangian Particle Dispersion Model (LPDM) described by Uliasz (1994) is used as the adjoint model of the WRF-FDDA modeling system. Particles are released from the receptors in a *backward in time* mode with the wind fields and the turbulence generated by the Eulerian model WRF-FDDA. In a *backward in time* mode, particles are released from the measurement locations and travel to the

surface and the boundaries. Compared to a forward mode, all the particles here are used to estimate fluxes, which reduces the computational cost of the simulation. Every 20 seconds, 35 particles are released at the position of the towers, which corresponds to 6,300 particles per hour per measurement site (or receptor). At high spatial resolutions, the particle locations have to be stored at a much higher frequency compared to regional applications. As a first estimation, a particle would fly over a 1km pixel in about 3 minutes (assuming a horizontal mean wind speed of 5 m/s). To avoid any gaps in the particle trajectories, particle positions were recorded every minute. At the opposite, because the domain is small (87km wide), the integration time, *i.e.* the time window during which the air masses are influenced by the local surface emissions, is limited to few hours. Here, particles were integrated over 12 hours to ensure that particles traverse the entire domain in any meteorological situations.

The dynamical fields in LPDM are forced by mean horizontal winds (u , v , w), potential temperature, and turbulent kinetic energy (TKE) from WRF-FDDA. At this resolution (1 km), turbulent motion corresponds to the closure of the energy budget at each time step. This scalar is used to quantify turbulent motion of particles as a pseudo random velocity. Based on the TKE, wind, and potential temperature, the Lagrangian model diagnoses turbulent vertical velocity and dissipation of turbulent energy. The off-line coupling between an Eulerian and a Lagrangian model solves most of the problems of non-linearity in the advection term at the mesoscale. Most of the non-linear processes resolved by the atmospheric model are attributed to a scalar representing the velocity of the particles. At each time step (here 20 seconds), particles move with a velocity interpolated from the dynamical fields of the WRF-FDDA simulation stored every 20 minutes. The time step depends on the TKE, following the discretization scheme described in (Thomson, 1987).

The formalism for inferring source-receptor relationships from particle distributions is described by Seibert and Frank (2004). At each time step, the fraction of particles (released from one receptor at one time) within some volume, gives the influence of that volume on the receptor. If the volume includes the surface this will yield the influence of surface sources. If the volume includes the boundary (sides or top) it yields the influence of that part of the boundary.

2.3 The INFLUX CO₂ observation tower network

The measurement network was described in (Miles et al., 2015) for CO₂, CH₄, and CO. Here, we used the daytime CO₂ mixing ratios (17-22 UTC) from nine of the twelve instrumented towers, corresponding to the sites operational between September 2012 and April 2013. The sites (1, 2, 3, 4, 5, 7, 9, 10, and 12) are presented in Figure 2. The Cavity Ring Down Spectrometer instruments (Crosson, 2008) measured the atmospheric CO₂ mixing ratios continuously over the period, at different sampling heights depending on the existing tower infrastructure. The minimum sampling height is 40m high at Site 10 and the maximum is 136m high at Site 2. The instruments were calibrated using the protocol described in Richardson et al. (2011), with a drift of less than 0.2 ppm per year across the sites, and a noise of 0.1 ppm on daily daytime averages (Miles et al., 2015).

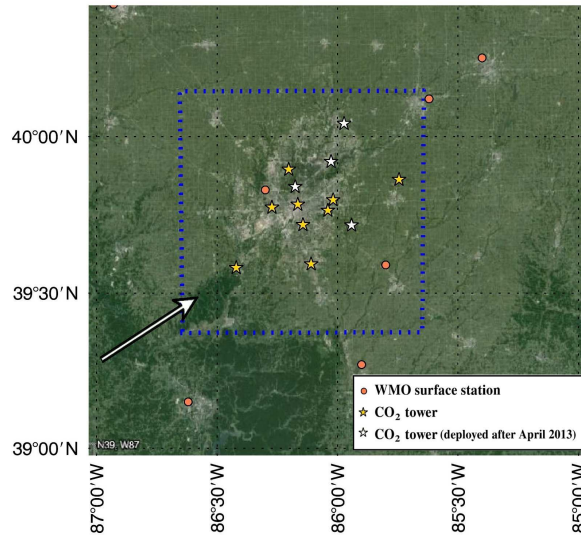


Figure 2. CO₂ tower locations (gold star) in the 1km simulation domain (blue square), with additional towers not available for the study period (white star), and surface meteorological stations (red circles) from the WMO database used in the WRF-FDDA modeling system. Indianapolis is located at the center of the domains.

2.4 Prior fluxes for CO₂

2.4.1 High resolution emissions: The Hestia product

The Hestia CO₂ emission product (Gurney et al., 2012) was coupled to the WRF-FDDA model to simulate the CO₂ atmospheric mixing ratios over and around Indianapolis. The Hestia product combines observations and modeling to produce CO₂ emissions from the combustion of fossil fuels, and is considered here as a "bottom-up" approach. A wide range of data sources are used to quantify emissions at the scale of individual buildings and road segments, including local traffic monitoring, property tax assessor data, power plant emissions monitoring, air quality pollution reporting. The data product includes some spatial and temporal proxies to attain hourly emissions at fine spatial scales for Marion county and the eight counties that surround Marion County. The space and time patterns are generated for the year 2011. Emissions for 2012 and 2013 reflect the application of scale factors derived from the DOE Energy Information Administration fuel statistics specific to sector and fuel type. Hence, the magnitude of emissions change over the 2011-2013 time period but the sub-county spatial structure remains fixed. Furthermore, the sub-monthly time structure in all sectors other than power production are represented by fixed time cycles derived from multiple years of monitoring data. For example, the onroad CO₂ emissions reflect a spatially-explicit use of a mean weekly cycle (7-day cycle within a given month) and mean diurnal cycle (24-hour cycle within a given week). The emissions available for each of the 8 economic sectors (cf. Table 1) for the

years 2012 and 2013 were aggregated from the initial building-level product down to 0.002 degree resolution. The 0.002 gridded product was then aggregated further at 1km resolution over the WRF grid, covering Marion county and the eight surrounding counties. Figure 2.4.2 (left panel) shows the CO₂ emissions in ktC.km⁻² from Hestia with the nine instrumented towers that were operational during the inversion period. The 1-km WRF grid was designed to cover the area corresponding to the 9 counties, except for a minor fraction extending beyond the rectangular domain. The total CO₂ emissions for the 9 counties around Indianapolis are 6.84 MtC for the year 2012 and 7.17 MtC for 2013. The 8-month total emissions over the inversion domain, representing most of the 9 counties slightly cropped following the WRF simulation domain, are 4.56 MtC for September 2012 to April 2013.

2.4.2 The Open-source Data Inventory for Anthropogenic CO₂ (ODIAC) emission data

We used the Open-source Data Inventory for Anthropogenic CO₂ (ODIAC) emission data (Oda and Maksyutov, 2011) as an alternative prior for inversion. The version of the ODIAC emission data used in this study is based on emission estimates updated using the CDIAC global and national fossil fuel emission estimates (http://cdiac.ornl.gov/trends/emis/meth_reg.html; last access 27 March, 2015) and the year 2013 edition of BP statistical review of world energy ¹. The emission spatial distributions were estimated at 1x1km resolution using the same method presented in Oda and Maksyutov (2011). The emissions from power plants are mapped using the geolocation reported in the CARbon Monitoring and Action (CARMA) global power plant database (www.carma.org; last access 27 March, 2015) and the rest of the emissions (non point source emissions) are distributed using the satellite observed nightlight data. The nightlight data used in the version of ODIAC emission data were developed using a new algorithm, improving the representation of suburban areas compared to the original version Oda et al. (2010). ODIAC emission data only indicates monthly emissions (based on CDIAC monthly emission data) and do not have diurnal and weekly cycles. Further details of the ODIAC are described in Oda (2015).

2.5 Prior emission errors

The complexity of the underlying model used to generate the Hestia emission product at very high resolution (*i.e.* building-scale) limits our ability to rigorously quantify the associated errors, including their spatial and temporal structures. As a simplified approach, we defined the error variances as a percentage of the net emissions for all the economical sectors, except for the utility sector for which the emissions are better constrained. Hourly energy production statistics and direct measurements provide more accurate hourly emissions for energy production (*i.e.* utility sector). Therefore, we defined the error variances as 60% of the net emissions at 1km resolution in the initial case for all the

¹<http://www.bp.com/en/global/corporate/about-bp/energy-economics/statistical-review-of-world-energy/statistical-review-downloads.html>; last access 27 March, 2015

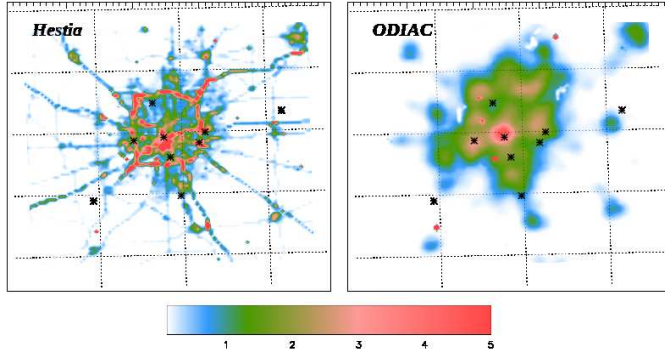


Figure 3. CO₂ a priori emissions using the Hestia product aggregated at 1km resolution (left) and the space-based emissions from ODIAC downscaled at 1km resolution (right)

sectors except the utility sector. Overall, the aggregated error variance is about 25% of the total emissions over the entire domain for each 5-day periods. We performed a second test with much larger prior errors (*i.e.* 100% of the net emissions) to evaluate the convergence of the inverse emissions in a very under-constrained system (cf. Section 4.4). For the spatial error structures, we used a similar approach to Lauvaux et al. (2012), *i.e.* a correlation length exponentially decaying with the distance, applied among urban pixels only (based on the National Land Cover Database 2010). The distance-based correlation matrix (C_L) is created first and then combined with land cover types for each land cover type assuming no correlation between urban and non-urban pixels (C_{urb}). The combined matrix is created assuming equal weights from both correlation matrices, using $C_f = \sqrt{C_L} \cdot \sqrt{C_{urb}}$. For the definition of the correlation length L , we tested the impact on the posterior emissions using varying distances, *i.e.* no correlation, $L=4\text{km}$ and $L=12\text{km}$. The use and the definition of correlation length in prior emission errors is discussed in section 4.4, and considered as an additional contribution to the overall uncertainties, mainly associated with the definition of the correlation length, in section 4.4.

The length of the inversion window was defined by the averaged length of synoptic and mesoscale events over the area. Typically, wind directions change with the passage of weather systems, which results in incomplete surface coverage in terms of tower footprints if the inversion time window is too short. The minimum of 5 days correspond to 2 to 3 synoptic conditions on average, and represent the minimum length to constrain the whole area. As we invert for 5-day emissions, temporal correlations are considered negligible between two inversion windows. To evaluate this assumption, we performed a similar inversion using 10-day periods and compare the results in section 3.6.

2.6 Observation errors

2.6.1 Observation error variances

250 For the transport model errors, we propagated the errors of the WRF-FDDA system into the inversion system through the error variances. The propagation of errors was performed in two steps: 1. we quantified the Mean Absolute Errors (MAE) at hourly time scales in WRF-FDDA using the available surface WMO stations to define the hourly performance of the model, and 2. we scaled the error variances using the normalized distance of a χ^2 distribution over each 5-day periods. This technique
 255 removes singular time steps during which the transport model performed poorly. The balance between prior error statistics and observation errors was evaluated using the χ^2 normalized distance λ , defined by $\lambda = \frac{1}{n}[(\mathbf{y} - \mathbf{H}\mathbf{x}_0)^T(\mathbf{H}\mathbf{B}\mathbf{H}^T + \mathbf{R})^{-1}(\mathbf{y} - \mathbf{H}\mathbf{x}_0)]$, similarly to Kaminski et al. (2001).

For the first step, the hourly MAE averaged over the domain, ε , for the wind speed and direction were used to define the hourly transport errors. Because these measurements were assimilated in
 260 the WRF-FDDA simulation, the true MAE is most likely under-estimated. However, we use these model-data residuals as a representation of the relative performances of the WRF-FDDA model at the hourly time scale. In principle, meteorological errors cannot directly be diagnosed from modeled CO_2 mixing ratios to describe the CO_2 variances in the inversion. Indeed, both flux and transport errors affect the simulated CO_2 mixing ratios. Instead, we only diagnosed transport errors from
 265 meteorological errors, which were then transformed into hourly scaling factors applied to hourly CO_2 variances. To quantify these scaling factors, an error model was created to generate transport errors for the CO_2 mixing ratios depending on both errors, *i.e.* in wind speed and direction. An adjustment coefficient defined as the ratio between the hourly MAE and the median of the MAE over the 5-day period was computed for both variables. The maximum of the two ratios define the
 270 hourly adjustment coefficient. To avoid using the time steps during which the model is inaccurate, the hourly errors were used to scale the variances $\varepsilon_{i,j}^2$ for a grid point (i,j) (*i.e.* the diagonal terms in \mathbf{R}) using the following relationship:

$$\varepsilon_{i,j}^2 = \max\left(\frac{\varepsilon_{spd}}{\mu_{spd}}, \frac{\varepsilon_{dir}}{\mu_{dir}}\right) \cdot \varepsilon_{init}^2 \quad (1)$$

with ε_{spd} and ε_{dir} the hourly mean errors, μ the median of the 5-day errors, and ε_{init}^2 the first-
 275 guess variance. The first-guess variance is our best-estimate computed from a χ^2 test (cf. 2.8) using the normalized distance λ over each 5-day periods (Tarantola, 2004). λ is constant for each 5-day windows, and is applied to correct for unbalanced error terms (ratio of prior emission errors to number of unknowns). The hourly scaling factors are applied to the first-guess variance corrected by λ . For non-diagonal matrices, as described in the next section, the normalized distance λ correction
 280 cannot be applied directly to the variances. Otherwise, the correction would be applied multiple times through the covariances and therefore over-estimate the total errors by several factors. In other terms, applying a multiplicative factor to the variances would amplify the scaling through the covariances.

To compensate for the over-estimation by the error covariances, we applied the square root of the scaling factor ($\sqrt{\lambda} \cdot \varepsilon_{i,j}^2$) which is assuming a linear relationship between variances and covariances
 285 ($cov_{x,y} = corr_{x,y} \cdot \sigma_x \cdot \sigma_y$). This technique was tested over multiple 5-day segments and produced a systematically better normalized distance λ (*i.e.* closer to one).

Over the inversion period (September 2012 to April 2013), the median of the wind speed MAE is about 0.8 m.s^{-1} and 12° . These two terms μ_{dir} and μ_{spd} were used for the inOn an hourly basis, the ratio between the median and the hourly MAE would define the adjustment of the initial error,
 290 *e.g.* multiplied by 2 for a wind speed MAE between 0.8 and 1.6 m.s^{-1} . We compared this method to using a constant $\varepsilon_{i,j}$ over time but no hourly adjustment based on the MAE in Section 3.6.

2.6.2 Observation error correlations

At high resolutions, spatial and temporal correlations in transport model errors become increasingly important. Past studies have approached the problem at coarser resolutions (*e.g.* Gerbig et al.
 295 (2003); Lauvaux et al. (2009b)) and found that error covariances are significant when the distance between observation locations is low. Using a diffusion equation model with an ensemble of transport simulations at 8-km resolution, Lauvaux et al. (2009b) estimated the averaged correlation length in transport model errors at about 30-40km. Between the INFLUX towers, the averaged distance is about 40km, which suggests that spatial error correlations may be significant. However, the correlation length may vary in space and time, and is likely to depend on model resolution and physics. To
 300 evaluate the sensitivity of the inverse emissions to spatial error correlations, we assumed a relatively small correlation length and an exponentially decaying model for the distance, with $L_{obs}=10\text{km}$, following the equation:

$$C_{obs}^{i,j} = \exp^{-\frac{d_{i,j}^2}{L_{obs}^2}} \quad (2)$$

305 with $C_{obs}^{i,j}$ the correlation coefficient between two tower locations i and j , and $d_{i,j}$ the distance between the towers i and j . The observation error correlation matrix C_{obs} has to be symmetric, positive semidefinite, with the diagonal terms equal to one. Further investigations of C_{obs} showed that a small number of eigenvalues were negative and required some modifications of the initial matrix before inversion. Following Brissette et al. (2007), we used an iterative process to filter negative
 310 eigenvalues. The negative values were replaced by slightly positive eigenvalues, and the correlation matrix was re-generated using the original eigenvectors. The matrix was slightly modified to be symmetric and with positive correlations only. The iterative process converged for all the inversion periods, modifying the correlation by less than 10%.

Temporal error correlations at high frequency (*i.e.* hourly) can also affect the simulated atmospheric mixing ratios (Lauvaux et al., 2009b). However, the batch inversion system as defined here
 315 is less affected by the impact of hourly error correlations, as the atmospheric data are assimilated in a single block. Spatially, emission corrections may still vary, but the overall city-wide emissions are

unlikely to be affected. Therefore, no temporal correlation was introduced in the errors. We quantified the impact of spatial error correlations by performing a sensitivity study, comparing the impact of error correlation, *i.e.* non-diagonal terms in \mathbf{R} to the initial configuration in section 4.1. Further investigation is required to define more completely the spatial and temporal error correlations in high resolution transport simulations and their impact on the inverse emissions, similar to Lauvaux et al. (2009b) at coarser resolution.

2.7 Boundary inflow: data selection

The constant flow of air through the boundaries of a limited-domain atmospheric simulation represents a significant amount of carbon compared to the local emissions, and therefore is a critical quantity that has to be characterized in the inversion system (Göckede et al., 2010; Lauvaux et al., 2012). Several studies have suggested to simply measure this quantity upwind of the metropolitan area (Kort et al., 2012; McKain et al., 2012) similar to aircraft mass-balance techniques (Cambaliza et al., 2014; Karion et al., 2015). However, background measurements can be affected by local fluxes and/or the local atmospheric dynamics which would impair its spatial representativity as a background measurement. The inflow of air follows primarily the wind direction and its variability in time and space, directly affecting our ability to measure the upwind conditions in any meteorological situations. Therefore, no measured background concentration would remain constant as the air moves across the domain. Advection-diffusion and vertical mixing modify the mixing ratios as air masses move over the city, increasing the representation errors associated with upwind measurements.

To measure the background air, the initial design of the Influx network included two sites covering the two major wind directions in the area, *i.e.* Site 1 for the north-westerly through westerly flows and Site 9 for northerly through easterly winds. Miles et al. (2015) compared several sites of the network (*i.e.* Sites 1, 4, 5, and 9) by computing the fraction of days corresponding to low atmospheric concentrations for each site. This analysis assumes that cleaner air should be measured at the background sites. The results indicate that Site 1 shows the lowest concentrations on average over time, whereas Site 9 is systematically biased by a couple tenths of a ppm. Sites 4 and 5 are clearly influenced by local emissions and should not be used as background sites.

We selected Sites 1 and 9 as our least biased background sites for our analysis and defined the background concentration for each hourly measurements over Indianapolis following different scenarios. These scenarios correspond to the definition of the upwind concentrations at a given time, or under specific conditions. To evaluate the impact of the definition of the boundary conditions on the inverse emissions, we produced several inverse emissions using different selection methods. First, we used a fixed site for the entire inversion period, using the hourly concentrations at the exact hour. This scenario is the simplest option for limited networks of towers. Second, we used an upwind model, selecting the sites based on the hourly surface wind direction in the center of Indianapolis.

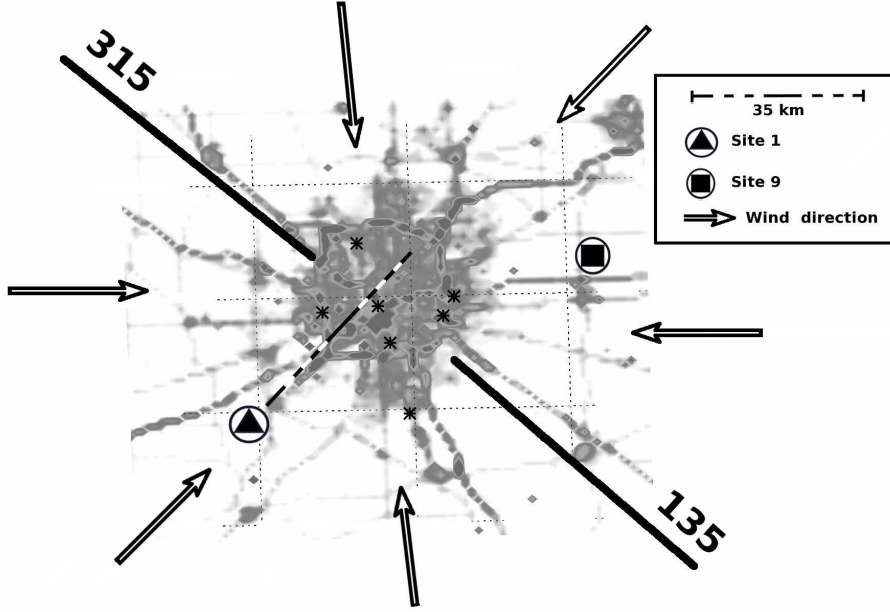


Figure 4. Selection of the background site to determine the upwind concentrations of CO₂ over Indianapolis, using two semicircles (135° and 315°) and hourly modeled wind directions from the WRF-FDDA system at three locations across the city. The emitting area defined by Hestia is represented in grey. The distance between Site 1 and Site 2 (about 35km) corresponds to an advection time of about 2 hours.

The upwind model selected Site 1 when the wind was between 135° and 315°, and Site 9 for 315°
 355 to 135° (cf. Fig. 4). Third, we used a daily minimum measured across the network to evaluate the importance of hourly changes. The results are presented in section 3.5.

2.8 Inversion methodology

The inversion system solves for a 5-day averaged emission vector of 87x87 unknowns as described in Tarantola (2004) by minimizing the cost function J and following the equation:

$$360 \quad \mathbf{x} = \mathbf{x}_0 + \mathbf{B}\mathbf{H}^T(\mathbf{H}\mathbf{B}\mathbf{H}^T + \mathbf{R})^{-1}(\mathbf{y} - \mathbf{H}\mathbf{x}_0) \quad (3)$$

where \mathbf{x} are the unknown emissions, \mathbf{x}_0 the a priori emission estimate, \mathbf{y} the observations, \mathbf{H} the influence functions, and \mathbf{R} and \mathbf{B} the uncertainty covariance matrices of the observations and the prior emissions respectively. We can define the posterior error covariance \mathbf{A} for sources given by the following expression $\mathbf{A}^{-1} = \mathbf{B}^{-1} + \mathbf{H}^T\mathbf{R}^{-1}\mathbf{H}$.

365 No diurnal cycle has been considered here as the advection of air masses across the domain takes less than 5 hours. With the first observation time being 17 UTC (12pm/1pm local time), the correction of the emissions applies only to daytime emissions (7am/8am). In other terms, nighttime

emissions cannot be constrained using daytime observations for such a small domain. For the total emissions presented in this study, the posterior emissions correspond to the inverse results for the period 12 - 22 UTC, combined with the prior emissions (Hestia) for the period 23 - 11 UTC. We performed a second case using a slightly different time window, *i.e.* 20 to 23 UTC, due to the lack of a precise definition of the afternoon, corresponding in theory to the well-mixed conditions in the PBL. We followed the optimal time window defined in Miles et al. (2015) to evaluate the sensitivity of the inverse emissions to the observation time window (cf. 3.6).

3 Results

3.1 Sectoral contributions

We show in Figure 5 the sectoral contributions at each tower locations based on Hestia 2012 emissions combined with the WRF-FDDA-LPDM footprints for the month of October 2012. The simulated CO₂ mixing ratios correspond to the 1-km surface footprints combined with the aggregated 1km Hestia emissions, at the hourly time scale, averaged over the month of October 2012 for the hours 17-22UTC. The atmospheric mixing ratios have not been normalized to reflect the impact of lower sampling heights on the magnitude of the atmospheric signals. This effect is simulated by the Eulerian and the Lagrangian models later in this study. The two sites with two lowest sampling heights (at 40m high) are the sites 10 and 12. Atmospheric enhancement at Site 12 is low despite the low sampling height. However, the enhancements at Sites 10 and 3 are large, mostly because of the presence of two power plants. The mobility sector, (*i.e.* traffic emissions), is the largest contributor to the atmospheric enhancements (45% of the total enhancements) at the nine tower locations, similar to the emission ratios for the same sector (44%). The second contributor is the utility sector, with two towers showing very large contributions (about 50%), and most the towers between 10 and 20% (except Site 9 with only 2% of the signals). In terms of emissions, the utility sector represents 20% of the emissions over the nine counties. This sector is clearly under-represented by most towers, over-represented at two sites (3 and 10), and absent at Site 9. The non-uniform distribution is explained by the locations of the power plants, *i.e.* with only few large point sources over the domain. Atmospheric signals from the industry sector represents about 12% on average, similar to its associated emission contribution of about 9%. The commercial and residential sectors represent respectively 6% and 9% of the atmospheric enhancements, compared to 6% and 7% of the emissions. Finally, the airport and the railroad sectors represent less than 2% each of the total signals, similar to the emission contribution.

3.2 CO₂ inverse emissions over Indianapolis (Initial configuration)

We present here the results for the initial configuration of the inversion system. Some of the assumptions made in this inversion are discussed later as additional unknowns. Here, the a priori emissions

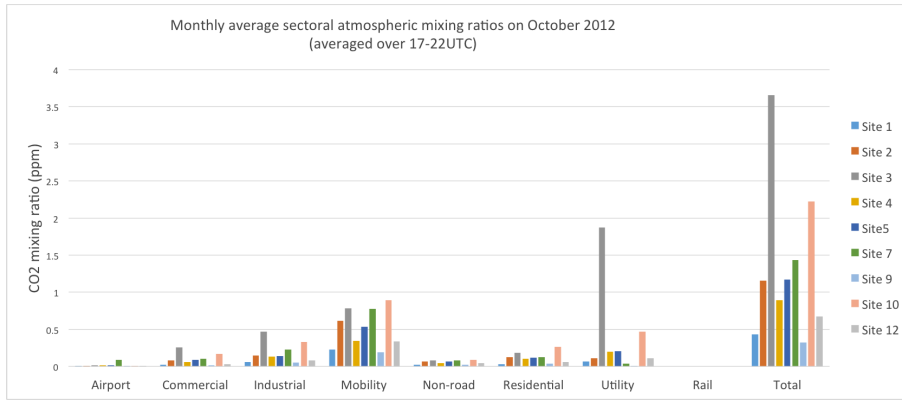


Figure 5. Sectoral contributions (in ppm) using the WRF-FDDA-LPDM footprints at 1km resolution combined with the Hestia sectoral CO₂ emissions for October 2012, except for the Railroad and the airport sectors representing about 2% of the emissions and the atmospheric enhancements.

Emission Sector	Com	Ind	Road	NonRoad	Res	Util
Atmos. signals	6%	13%	45%	5%	9%	20%
Surface Emiss.	6%	9%	44%	6%	8%	20%

Table 1. Sectoral contributions (in %) in the simulated tower mixing ratios averaged over the network of 9 towers compared to the surface CO₂ emissions (Hestia).

correspond to the Hestia emissions aggregated at 1km resolution. The prior errors were set to 60% of the net emissions, including an urban correlation length of 4km to define the spatial error structures as described in section 2.5. The background mixing ratios were defined by the observed mixing ratios at Site 1 (SW of Indianapolis). Figure 6 shows the CO₂ emissions time series averaged over 5-day periods from Hestia (upper panel, in red) and the corresponding posterior emissions (upper panel, in blue) from September 2012 through April 2013. The errors for each 5-day estimate are significantly reduced after inversion, from about 25% to around 9% on average. Over the 8-month period, the inverse emissions remain similar to the a priori Hestia emissions, with some additional variability.

The emissions are increased during the first few months (September to mid November). The total aggregated emissions are about 20% higher than the Hestia emissions over the period (5.5MtC versus 4.56MtC). The emission corrections are shown in Figure 7 (lower left panel) with an overall increase following the beltway and the residential and commercial areas. The error reduction (upper

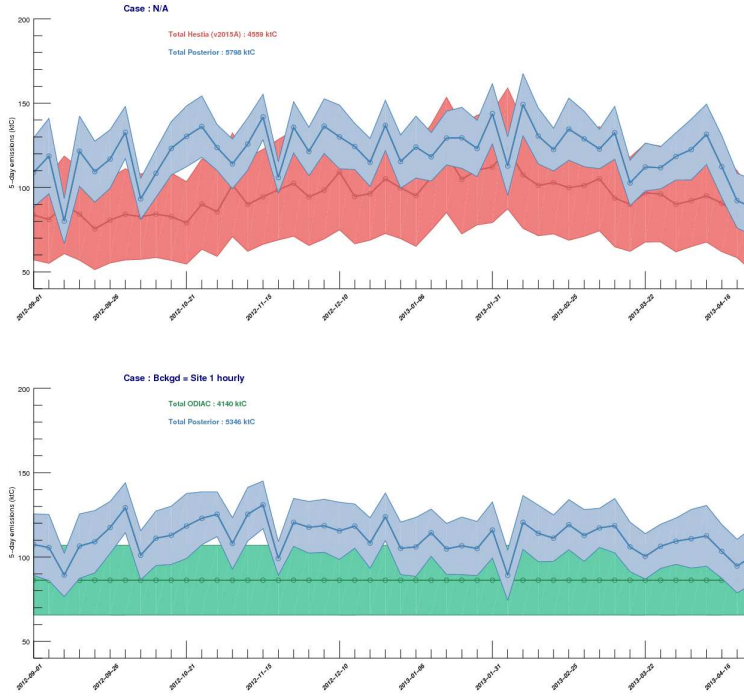


Figure 6. 5-day inverse emission estimates in ktC for Hestia (upper panel, in red), ODIAC (lower, in green), and their respective inverse emissions (in blue) for the period September 2012 - April 2013

left panel) is about 30% in the urban area, with larger values in the southern part of town, where the tower density is higher (cf. Fig. ??).

3.3 Impact of a priori emissions (ODIAC)

The ODIAC CO₂ emissions were used as a priori emissions, which also impacts the prior emission errors due to the scaling of the variances with the net emissions. In addition, a larger error was used for ODIAC, *i.e.* 100% at the 1-km pixel level. Figure 6 shows the 5-day emissions from ODIAC (lower panel, in green) and the corresponding inverse emissions (lower panel, in blue). The temporal variability in the inverse emissions shows some differences compared to the initial case, which suggests that the spatial distribution of the prior emissions and their associated errors can impact the temporal variability of the inverse solution. However, the variability remains similar to the initial case, with lower emissions around the end of 2012 and early 2013. The error reduction presented in Figure 7 (upper right panel) shows a homogeneous reduction of about 30%, driven primarily by the homogeneous variances and the spatial error correlations, and covering a larger surface extent than the Hestia-based inversion estimate. The emission corrections (lower right panel) are similar to the error reduction spatial distribution. These results suggest that the assumed correlation length over

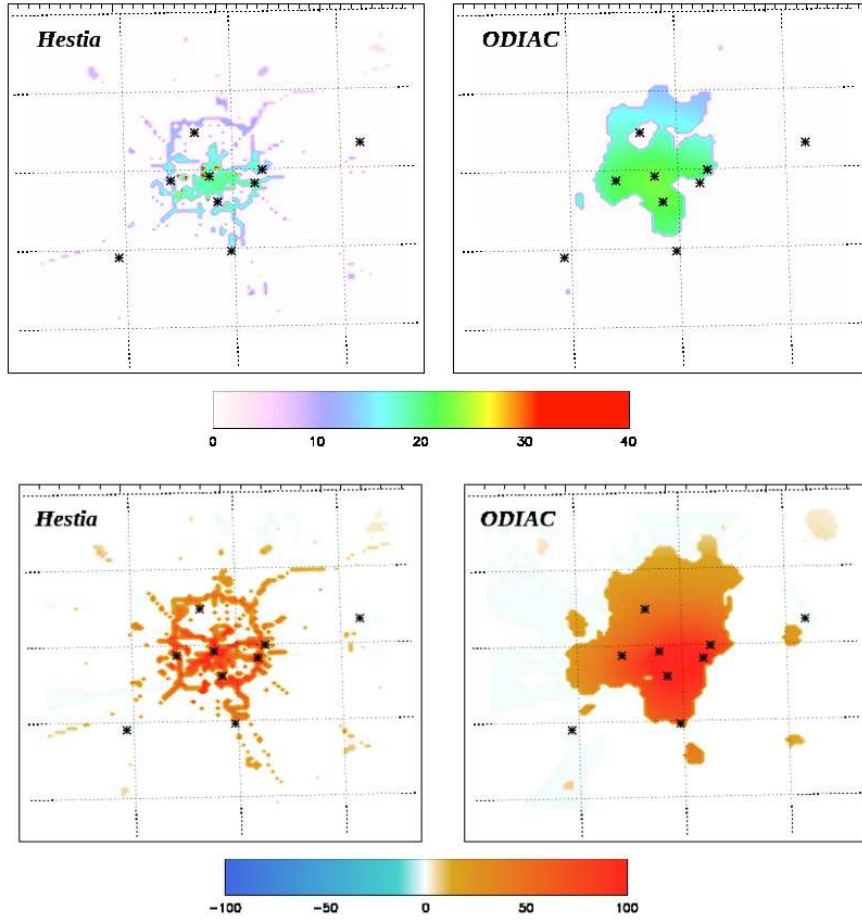


Figure 7. Error reduction (in %) (upper panels) and relative change in emissions after inversion (in %), *i.e.* differences between the prior and the posterior emissions (lower panels), using the Hestia product (left) and ODIAC (right) as prior emissions

the urban area forces the spatial distribution of the inverse emissions rather than the variances. Otherwise the corrections would be larger in the downtown area. We present three other cases in section 4.4, and discuss the current limitations due to the absence of well-characterized error structures in the prior emissions. The total emissions are indicated in Table 2 with an a prior total of 4.14MtC, slightly lower than Hestia, and an inverse estimate of 5.4MtC, larger than inverse estimates using Hestia. The assumptions in the prior errors drive to a large extent the larger emission correction when using ODIAC, considering that ODIAC errors are larger than Hestia.

3.4 Transport model errors: scaling of variances

The atmospheric simulations using the WRF-FDDA modeling system were evaluated using three meteorological surface stations in the Indianapolis area for both the horizontal mean wind speed and direction. The PBL depth evaluation over two months (September-October 2013) was used to select the model physics configuration and quantify the impact of the meteorological assimilation system (Deng et al., in prep.). Over a 2-month period, the simulated PBL depths were compared to observations from a HALO Photonics Doppler lidar². HALO measures high-resolution vertical velocity variance and aerosol backscatter signal strength profiles that can be used to measure the mixing depth. The systematic model-data mismatch (mean error) is 105 m over the two months, and the mean absolute error is 275 m. These mismatches are relatively small over the 2-month period corresponding to less than 7% of the PBL depth. Considering model performances at higher frequencies (hourly to daily variability), we used surface wind measurements to quantify the hourly variances as a first-order assessment of model errors. The PBL depth was not used to estimate model errors at the hourly time scale. In urban environments, the spatial gradients in emissions are extremely large compared to natural ecosystems. Therefore, wind errors can affect significantly the spatial distribution of the inverse emissions if a large source is attributed to a near-zero emission area. To describe hourly model errors, we used wind direction and speed as proxies in order to propagate model errors into the inversion and avoid source attribution errors.

Wind speed and direction model-data differences were used to scale the hourly errors (*i.e.* the variances in the observation error covariance matrix \mathbf{R}) associated with the modeled mixing ratios. The monthly statistics for both variables are shown in Figure 8 with the quartiles of the mean error, and the median of the mean absolute errors over each month. Whereas the hourly variability (represented by the 25% and 75% quartiles) is large, the monthly medians are low (about 12.2° for wind direction and 0.8ms^{-1} for wind speed over the entire period). These results suggest that whereas monthly systematic transport errors are small, the hourly errors can be large. The simulated meteorological conditions can be off by 45 degrees or more for a specific observations. We corrected for hourly errors by introducing the hourly wind errors in \mathbf{R} (diagonal elements) as explained in section . When using the scaling of the variances of the observations based on model transport errors, the inverse emissions aggregated over the period decrease slightly compared to the initial case (5.73MtC versus 5.79MtC (cf. Table 2).

Overall, the WRF-FDDA system improves significantly the averaged performance of the WRF atmospheric model compared to the historical mode (*i.e.* no assimilation of meteorological data), as shown in Rogers et al. (2013). For this second step, *i.e.* propagating hourly variances into the inversion system, which is equivalent to filtering the transport model results, the impact is less significant over the entire time periods. Errors associated with specific meteorological events have been considerably reduced by removing specific days. But over the 8-month time period, no bias has been

²<http://www.esrl.noaa.gov/csd/projects/influx/>

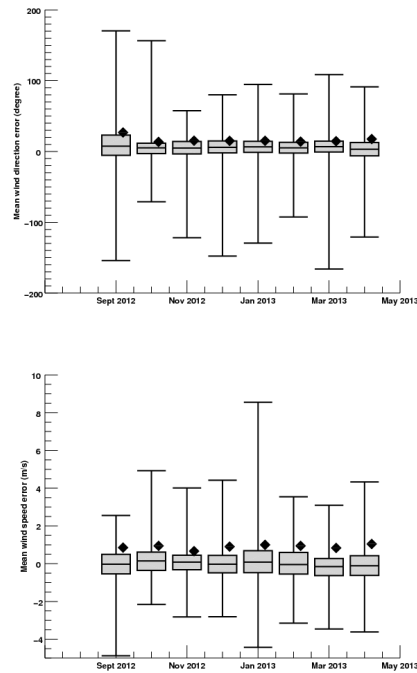


Figure 8. Quartiles of the monthly mean error and mean absolute errors (black diamond) for the horizontal mean wind direction (top panel) and speed (bottom panel) at 1km resolution using measurements from WMO surface stations.

associated with the hourly transport errors. This analysis suggests that long-term model improvements are more important than propagating short-term model deficiencies to avoid misattribution of hourly signals.

475 3.5 Sensitivity to the background concentrations

We present here the results of the different strategies used to define the background concentrations. The first strategy defines the background concentrations by using the concentrations at Site 1 at the exact time of the observations. Site 1 is the climatological background site located upwind about 60% of the time. The second strategy uses the optimal site location based on the wind direction (upwind
480 model), as described earlier. Sites 1 and 9 are the two options depending on the wind direction. When one site is not operational, the other is used even if the wind direction is not optimal. The last strategy uses the daily minimum at the upwind site, similar to the second strategy. This last option offset potential temporal variations observed in the early afternoon. The risk of sampling low concentrations at later times is not negligible. This strategy is the least likely option for realistically
485 sampling the background. Table 2 shows that the two first strategies produce very similar inverse total

Case	L=12km	Low traffic	Low utility	Large σ_B^2	ODIAC	L=4km
Prior	4.56	4.15	4.2	4.56	4.14	4.56
Posterior	5.79	5.16	5.24	6.13	5.35	5.5
Case	Wind model	Daily Min	10 days	$\lambda.\varepsilon$	20-23UTC	L=0km
Prior	4.56	4.56	4.56	4.56	4.56	4.56
Posterior	5.53	6.	5.88	5.73	5.69	4.73
Case	4 Sites (A)	4 Sites (B)	4 Sites A (L=4km)	4 Sites B (L=4km)		
Prior	4.56	4.56	4.56	4.56		
Posterior	5.36	5.52	5.13	5.17		

Table 2. Prior and posterior emissions from the various inversion configurations referred as the initial inversion case (L=12km), a decrease of 40% in the a priori traffic emissions (Low traffic), a decrease of 40% in emissions from the a priori energy production sector (Low utility), using large prior emission variances (Large σ_B^2), using ODIAC as prior emissions (ODIAC), assimilating only 4 sites out of 9 (4 Sites (A) and 4 Sites (B)), assimilating only 4 sites out of 9 with a lower correlation length of L=4km (4 Sites A (L=4km) and 4 Sites B (L=4km)), varying the correlation length L in the prior emissions errors (L=0km and L=4km), varying the definition of the background conditions using the wind direction (Wind model) or the minimum of the day (Daily Min), assimilating over a 10-day time window instead of 5 days (10 days), filtering hourly observations using wind model errors ($\lambda.\varepsilon$), and varying the afternoon window for observations (20-23UTC)

emissions with 5.53 MtC (wind model) and 5.5 MtC (L=4km), whereas the third strategy increases the total emissions significantly (6 MtC). The daily minimums are selected over the time window 17-22UTC, with the lowest values being usually observed between 20 and 22UTC. This technique introduces a positive bias in the inverse solution by selecting a late afternoon mixing ratios at the upwind site (*i.e.* lower concentrations), artificially increasing the emissions over the city. This last method is also the least realistic because the lowest concentrations are often observed at the end of the day, which is inconsistent with the advection time of air masses across the city. The first two strategies represents the difference between Site 1 and a combination of Site 1 and Site 9 depending on the wind direction. If Site 1 is contaminated by any local signals, the current analysis would not diagnose its impact. An additional site measuring background concentrations will be deployed to test the potential impact of upwind sources.

3.6 Uncertainty assessment: ensemble approach of inverse estimates

An ensemble approach of inversion configurations was designed to quantify systematic errors due to the various assumptions made in the urban inversion system. The ensemble consists of two sets of results, the first representing prior-related cases, such as varying the spatial error structures in prior emission errors, and the second set of results related to the observations and their associated

uncertainties. The first set of results, presented in Figure 9 (light gray), show three different correlation lengths L (as described in Section 2.5) and a different prior (ODIAC). The impact of various L is clearly the main contributor to the changes in total emissions, even if the fully uncorrelated prior emission scenario seems very unlikely considering the use of data and model parameters in the Hestia and ODIAC products. We discuss the impact of L on the spatial distribution and the total emissions in section 4.4. The use of ODIAC is also important with noticeable differences in the spatial distribution. The second set of results, in gray, includes different assumptions related to the time window for the observations (20-23UTC instead of 17-22UTC). Miles et al. (2015) defined the well-mixed conditions based on the temporal variability in the CO_2 mixing ratios, and found that the period 20-23 UTC would be more appropriate to avoid a late morning transition in the PBL depth. The results are presented in Table 2. The difference with the initial case remains small which may suggest that the WRF-FDDA model is able to simulate the late PBL growth in the early afternoon. The ensemble includes several other configurations including the use of hourly transport errors based on hourly wind error statistics, and the definition of the background concentrations. The two sets were used to define the quartiles of the ensemble, noted *ensemble spread* in Figure 9. The ensemble mean is about 5.66MtC, the second and third quartiles at 0.23MtC from the mean, the first and fourth quartiles at 0.85MtC from the mean. The inverse emission using Hestia and ODIAC are statistically different from the 50-75% of the ensemble mean. However, the definition of the correlation length seems to encompass both prior and posterior solutions, especially between no correlation in prior emission errors and the case $L = 4\text{km}$. We discuss the sensitivity to the prior error structures in section 4.4. The third set of results exploring network design cases and sectoral emissions, in Fig. 9 (dark gray), were not included in the ensemble and are discussed later in Section 4.3.

The time series presented in Figure 10 was created by the same two subsets of configurations (excluding the top 6 cases presented in Figure 9 in dark gray). In Fig. 10, the dark grey zone represents the ensemble spread whereas the light gray zone includes the ensemble spread and the posterior uncertainties of the cases. Earlier findings described in the time series of the posterior emissions (cf. Section 3.2) are confirmed here in the ensemble, with higher emissions than the Hestia prior (dashed line) during the first 3 months of the period, lower emissions at the end of December 2012 and early in January 2013, and an overall agreement in the first months 2013. Some short-term variations are consistent across the different configurations, *e.g.* the large increase in late October 2012.

4 Discussion

4.1 Impact of transport errors at high resolution

Urban emissions is likely to require the development of high resolution inversion system, potentially reaching the physical limits of the numerical scheme assumptions in the mesoscale model, such as the turbulence closure scheme in the PBL. In other terms, the risk of violating the parameterized

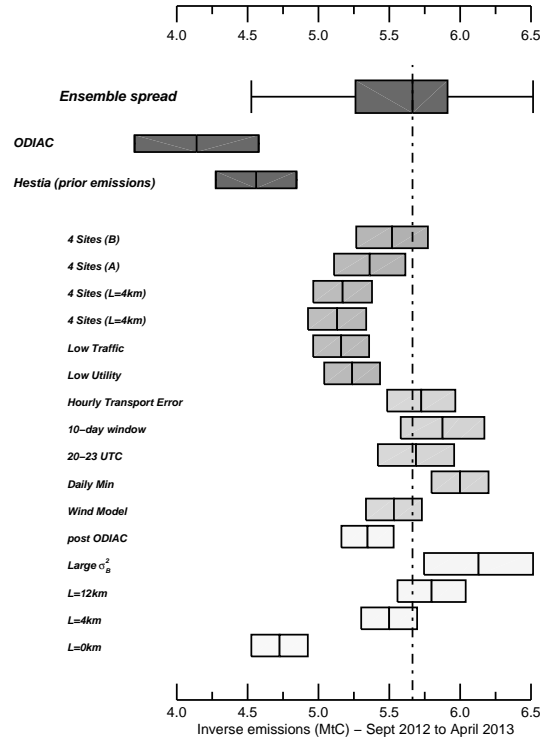


Figure 9. Whole-city inverse emission estimates in MtC over September 2012 - April 2013 using the different inverse system configurations and prior emissions

sub-grid scale turbulence assumption becomes non-negligible in stable and neutral conditions with turbulent eddies smaller than the model resolution. At short distances, the plume structures from isolated sources may not follow the well-mixed assumptions of the model. In addition to physical limits in numerical schemes, the local atmospheric dynamics is influenced by large spatial gradients in the surface energy fluxes. Under these conditions, sources of systematic errors in the transport model are numerous and difficult to overcome. The use of a meteorological assimilation system, *i.e.* WRF-FDDA, improves the model performances (Rogers et al., 2013) but large discrepancies can still affect the wind direction and speed (cf. Figure 8). Additional evaluation of the near-field atmospheric dynamics is still required to quantify the modeling performances and the representation of fine-scale structures, mostly visible around the major sources at short distances. Here we improved our initial WRF modeling system with the FDDA methodology, and propagated errors into the inversion scheme. We evaluated the impact of the spatial structures in the transport model errors through

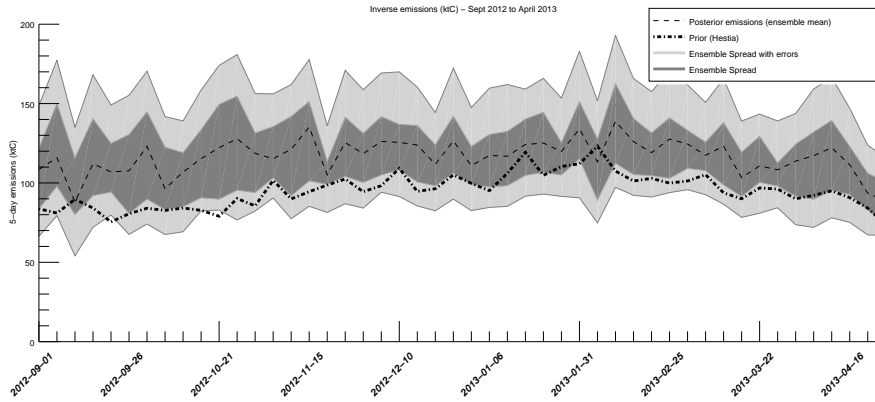


Figure 10. Ensemble of 5-day inverse emission estimates in ktC using multiple configurations, *i.e.* varying the prior error correlation length, the background definition, or the transport model errors, from September 2012 to April 2013

the use of correlation lengths, similar to (Lauvaux et al., 2009a) who diagnosed structures from a small ensemble of perturbed simulations. In this study, the correlation length scale was applied to the observation error covariance matrix with an exponentially decaying model. Considering the use of our high resolution WRF-FDDA simulation over a highly heterogeneous landscape, we reduced the length scale from 30km (in the original study) to 10km to represent the potentially smaller spatial structures in transport errors. When introducing these covariances, the posterior emissions end up at 4.93MtC, with a smaller correction to the prior emissions compared to the reference inversion, as expected when increasing the errors associated with observations. This initial inversion shows the importance of potential error structures at fine scales. No temporal correlation was introduced due to the lack of information at these scales and the batch inversion system which limits the impact of hourly error correlations.

4.2 Network design: impact of tower locations and heights

4.2.1 Network design of surface towers

The deployment of tower networks for emission monitoring highly depends on the objectives of the study. We propose here to discuss the monitoring of the emissions from the entire urban area, and the mapping of emissions at higher resolutions. For the first objective, we compare two sub-networks, presented in Table 2, which correspond to two optimal network configurations with one upwind site, one downwind site, and three centrally located towers. We also used two different correlation lengths ($L=4\text{km}$ and $L=12\text{km}$) in the prior error statistics as this parameter can significantly impact the inverse solution (cf. Section 4.4). By assuming a larger correlation length ($L=12\text{km}$), the two networks produce fairly different total emissions with 5.36MtC and 5.52MtC, which are further

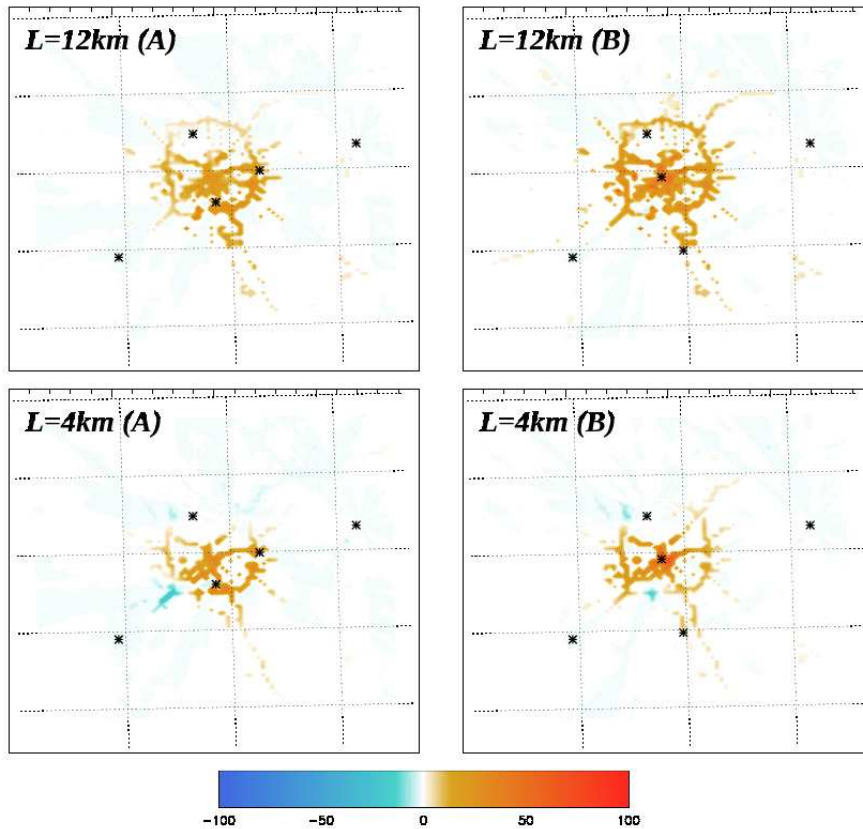


Figure 11. Emission correction (in %), corresponding to the ratio of emission change between the prior and the posterior emissions, for 2 different sub-networks. Both networks include 4 tower locations selected for both maximum enhancements over the city and background sampling. Both inversions were performed over the period September 2012 - April 2013, using the initial configuration.

decreased with lower L (respectively 5.13MtC and 5.17MtC). Figure ?? shows that the main difference between the two networks (left column compared to the right column) originates from the magnitude of the correction in the center of the city and a short section of the beltway (SW and N sections) which shifted from a negative correction (lower left panel) to a positive correction (lower right panel). The impact of the correlation length (4km versus 12km) is similar to the results using the entire network (cf. Figure 13), confirming that prior emission error structures do not only alter the total emissions but also the location of the sources, as discussed in Section 4.4. Overall, the tower deployment is highly dependent on the assumptions made in the prior emission errors. If large correlations are to be true, a network of four towers would suffice to constrain the urban emissions. But this assumption is highly uncertain, meaning that network design will require a better understanding and a better quantification of prior error structures before any robust conclusions can be made.

4.2.2 Sampling heights: Sensitivity to surface emissions

The various GHG analyzers deployed around the Indianapolis area are all on tower structures, with four instruments at 120m or more, four on 60-90m towers, and four at about 40m high. The sampling height remains a critical parameter in the mesoscale models, with large vertical gradients in stable to neutral stability conditions that are difficult to simulate correctly. In well-mixed conditions, 40m towers may still be affected by vertical gradients in the surface atmospheric layer, and very likely to suffer from large model errors. The Atmospheric Surface Layer (ASL) is not well-simulated in mesoscale systems, and at this elevation, even higher vertical resolution is unlikely to improve the vertical mixing near the surface. In Figure 12, we show the influence functions for the nine towers used in this study. Towers 1 and 9, located outside of the city to the West and the East of the network respectively, have a smaller impact on the surface emissions. These two towers are the tallest structures instrumented for the experiment, at 136m and 121m high. The WRF-LPDM footprints represent the increased sensitivity to the surface when the stability conditions are not convective. Because the inversion period covers winter, observations in the afternoon are still affected by vertical gradients in CO₂ despite selecting the period of maximum solar radiation. At these low elevations above ground-level, vertical gradients can be observed as shown in Miles et al. (2015). Further studies are needed to estimate the capability of mesoscale models to simulate correctly the vertical gradients in the ASL during well-mixed, stable, and neutral periods.

4.3 Sectoral emission detection and quantification

In the current study, the emissions over Indianapolis metropolitan area were inverted using the total CO₂ concentrations, *i.e.* without any consideration for the underlying emission processes. In section 3.1, the sectoral contribution is presented in the simulated mixing ratios, using the forward simulations. To investigate the potential of detection of the major economical sectors in the inversion, *i.e.* traffic and energy production, we performed two additional inversions decreasing the emissions from these two sectors, by 40% for the utility sector and by 20% for the traffic sector. The total prior emissions decreased from 4.56MtC originally to 4.2MtC and 4.15MtC (cf. Table 2). The inversion was able to retrieve most of the decrease, ending at 5.24MtC and 5.16MtC respectively. For the utility sector, the inverse solution distributed the correction according to the spatial structures in prior emission errors (not shown here), failing to identify precisely where the power plants were located. When assuming no spatial correlation in prior emission errors, the main emission correction was located in the South West quadrant of town, around the main major power plant (Harding Street). For the low traffic scenario, the spatial pattern of the emission correction matches the beltway, even though the pattern may be primarily constrained by the prescribed variances associated with traffic emissions. This first order assessment of emission detection suggests that the inversion system is

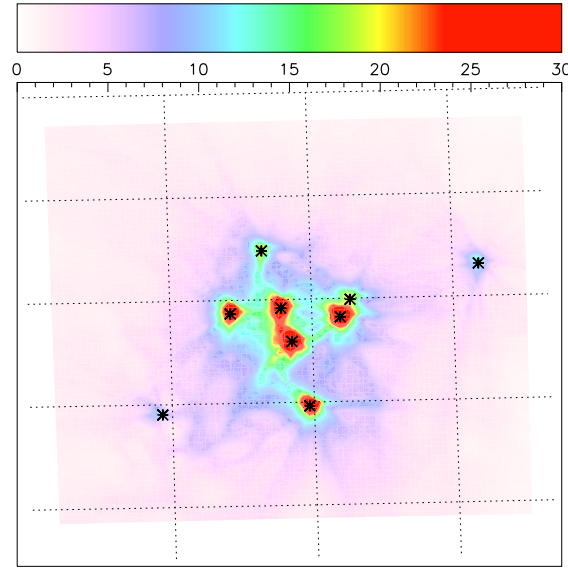


Figure 12. Influence functions in $\text{ppm}/(\text{gC.m}^{-2}.\text{h}^{-1})$ for the nine instrumented INFLUX towers aggregated over the 8-month period. Sites 1 and 9 show the lowest sensitivity to the surface primarily due to higher sampling heights under low vertical mixing conditions. Additional effects on shorter tower sensitivity due to the proximity of the sources is not considered here.

able to retrieve major changes in sector emissions. Additional investigations are needed to define the exact potential of the system for both trend detection in specific sectors and spatial variability.

4.4 Impact of prior error statistics on inverse emissions

The definition of the prior emission errors remains subjective at this point, with no existing rigorous quantification of emission errors at high resolutions. We used the difference between several existing emission products (*i.e.* Hestia and ODIAC) at the pixel-level to define the prior error variances, equivalent to 25% of the net emissions aggregated over the domain. At the pixel level, this corresponds to an uncorrelated error of about 60% for Hestia. We increased this error to 200% to generate a purely data-driven solution, with a low correlation length of 4km. The inverse emissions aggregated over the domain are equal to 5.57MtC compared to 5.5 MtC over the same time period for the initial case. The two solutions remain similar despite the very large prior emissions error. This results confirms that the total prior errors do not over-constrain the inverse solution. But solving for spatial structures across the area requires additional information related to the spatial structures of the prior emissions errors Saide et al. (2011). Methodologies to define the error structures exist (*e.g.* Wu et al. (2013)), assuming that simple parameters can be optimized, such as a correlation length in an exponentially decaying scenario. Here, the use of correlation length over the urban area increases

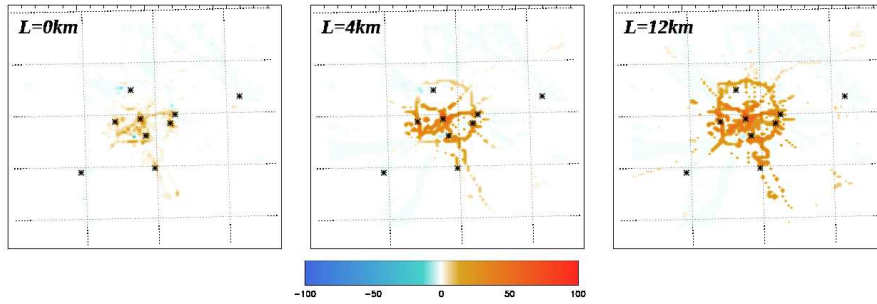


Figure 13. Relative change in emissions after inversion (in %) using no correlation length (left), a correlation length of 4km within the urban area (middle), and 12km within the urban area (right) in the prior emission error covariances

the complexity of such a model. But this approach was assumed to better represent the spatial coherence of incorrect emission factors for the mobility sector, or any systematic errors affecting the underlying models used in the Hestia emission product. A simpler model would ignore the urban area and potentially propagate corrections to non-urban areas. In Figure 13, we show the difference between the inverse emissions and the prior, using three different correlation lengths, *i.e.* $L=0km$ (left panel), $L=4km$ (middle panel), and $L=12km$ (right panel). The spatial distributions vary from localized adjustments around the sites (for $L=0km$), to an overall adjustment of the road emissions when assuming large correlations ($L=12km$). Clearly, the spatial distribution of the flux corrections are driven by the prior emission error structures. In addition, the total emissions vary from a minor correction (4.73MtC with $L=0km$), to more important corrections (5.5MtC and 5.79MtC with $L=4km$ and $L=12km$). Therefore, the quantification of prior emission errors and their associated structures is a critical component of the information. The correlation length impacts the total inverse solution and the spatial distribution of the solution, which relates to the sectoral attribution problem, as the structures dictate the distribution over different areas of the city. One could argue that no correlation in the prior emission errors may be an extreme case, considering that the underlying models used in the emission products such as Hestia combine emission factors with their input data. Therefore, spatial correlations would be likely to affect the emissions for specific combustion processes but not across the city as whole. Knowing that CO_2 emissions combine several sectors of activity which are unrelated for the most part, spatial structures in emission errors may be spatially limited once combined into total CO_2 prior emissions. For these reasons, future studies will need to address carefully this key parameter in the inversion system. Similar work has been accomplished at the regional scales, using optimization methods such as (Wu et al., 2013).

5 Conclusions

This study presents a high resolution inversion system based on a Four Dimensional Data Assimilation meteorological system to simulate the atmospheric dynamics at 1km resolution over the city of Indianapolis. The inverse emissions were evaluated over 8 months (*i.e.* September 2012 to April 2013) using two different a priori emissions, Hestia, a state-of-the-art building-level emission products, and ODIAC, a space-based emission product. The reference inversion produced whole-city inverse emissions of 5.5 MtC, about 20% higher than the prior emissions from Hestia (4.6 MtC). Total CO₂ emissions for the Indianapolis urban area based on the ensemble mean and quartiles are 5.26 - 5.91 MtC, *i.e.* a statistically significant difference compared to the two prior total emissions of 4.1 to 4.5 MtC. Single configurations of the inversion system produced lower posterior uncertainties than the ensemble spread, reflecting the uncertainties associated with the various assumptions. Transport model errors were estimated from the WRF-FDDA system and introduced in the inversion system through the use of hourly variances adjusted according to the hourly model performances. The upwind conditions were prescribed by using two towers located at about 20 to 30km from the city, with an hourly site selection based on wind observations. However, several parameters of the inverse system remain under-constrained, at the origin of the ensemble variability. In particular, spatial structures in prior emission errors, mostly undetermined, affect significantly the spatial pattern in the inverse solution, as well as the carbon budget over the urban area. We therefore conclude that atmospheric inversions are able to constrain the carbon budget of the whole city to an absolute uncertainty of about 25%, but additional information on prior emissions and more specifically about their associated error structures are required if atmospheric inversion systems are built to determine the spatial structures of urban greenhouse gas emissions at high resolutions.

6 Author contribution

T. Lauvaux performed the inversions; A. Deng performed the WRF-FDDA model simulations; B. Gaudet provided support for the WRF model evaluation; N. Miles and S. Richardson provided the calibrated tower greenhouse gas measurements; C. Sweeney, J. Turnbull, and A. Karion provided flask data for calibration and provided comments about the study; M. Cambaliza provided comments about the study; K. Gurney, J. Huang, I. Razlivanov, R. Patarasuk developed and prepared the Hestia emission product; D. Sarmiento contributed to model developments and improvement of the WRF model simulations; K. Wu contributed to the development of the inversion system; T. Oda provided the ODIAC emission product; K. Davis and P. Shepson provided comments and discussed the results of the study.

Acknowledgements. This work has been funded by the National Institute for Standards and Technology (project number 70NANB10H245), and the National Oceanic and Atmospheric Administration (Grant number NA13OAR4310076).

We also want to acknowledge the NOAA Earth System Research Laboratory Chemical Sciences Division for providing HALO lidar data.

References

- 690 Andres, R., Boden, T., and Higdon, D.: A new evaluation of the uncertainty associated with CDIAC estimates of fossil fuel carbon dioxide emission, *Tellus B*, 66, <http://www.tellusb.net/index.php/tellusb/article/view/23616>, 2014.
- Andres, R. J., Marland, G., Fung, I., and Matthews, E.: A $1^\circ \times 1^\circ$ distribution of carbon dioxide emissions from fossil fuel consumption and cement manufacture, 1950-1990, *Global Biogeochem. Cycles*, 10, 419–429, 1996.
- 695 Andres, R. J., Boden, T. A., Bréon, F.-M., Ciais, P., Davis, S., Erickson, D., Gregg, J. S., Jacobson, A., Marland, G., Miller, J., Oda, T., Olivier, J. G. J., Raupach, M. R., Rayner, P., and Treanton, K.: A synthesis of carbon dioxide emissions from fossil-fuel combustion, *Biogeosciences*, 9, 1845–1871, doi:10.5194/bg-9-1845-2012, <http://www.biogeosciences.net/9/1845/2012/>, 2012.
- 700 Asefi-Najafabady, S., Rayner, P. J., Gurney, K. R., McRobert, A., Song, Y., Coltin, K., Huang, J., Elvidge, C., and Baugh, K.: A multiyear, global gridded fossil fuel CO₂ emission data product: Evaluation and analysis of results, *Journal of Geophysical Research: Atmospheres*, 119, 10,213–10,231, doi:10.1002/2013JD021296, <http://dx.doi.org/10.1002/2013JD021296>, 2013JD021296, 2014.
- Bréon, F. M., Broquet, G., Puygrenier, V., Chevallier, F., Xueref-Remy, I., Ramonet, M., Dieudonné, E., Lopez, M., Schmidt, M., Perrussel, O., and Ciais, P.: An attempt at estimating Paris area CO₂ emissions from atmospheric concentration measurements, *Atmospheric Chemistry and Physics*, 15, 1707–1724, doi:10.5194/acp-15-1707-2015, <http://www.atmos-chem-phys.net/15/1707/2015/>, 2015.
- 705 Brissette, F., Khalili, M., and Leconte, R.: Efficient stochastic generation of multi-site synthetic precipitation data, *Journal of Hydrology*, 345, 121 – 133, doi:<http://dx.doi.org/10.1016/j.jhydrol.2007.06.035>, <http://www.sciencedirect.com/science/article/pii/S002216940700385X>, 2007.
- 710 Cambaliza, M. O. L., Shepson, P. B., Caulton, D. R., Stirm, B., Samarov, D., Gurney, K. R., Turnbull, J., Davis, K. J., Possolo, A., Karion, A., Sweeney, C., Moser, B., Hendricks, A., Lauvaux, T., Mays, K., Whetstone, J., Huang, J., Razlivanov, I., Miles, N. L., and Richardson, S. J.: Assessment of uncertainties of an aircraft-based mass balance approach for quantifying urban greenhouse gas emissions, *Atmospheric Chemistry and Physics*, 14, 9029–9050, doi:10.5194/acp-14-9029-2014, <http://www.atmos-chem-phys.net/14/9029/2014/>, 2014.
- Crosson, E. R.: A cavity ring-down analyzer for measuring atmospheric levels of methane, carbon dioxide, and water vapor, *Applied physics B*, 92 (3), 403–408, 2008.
- Deng, A., Stauffer, D., Gaudet, B., Dudhia, J., Hacker, J., Bruyere, C., Wu, W., Vandenberghe, F., Liu, Y., and 720 Bourgeois, A.: Update on WRF-ARW end-to-end multi-scale FDDA system, *WRF Users' Workshop 2009*, Boulder, CO, 2009.
- Deng, A., Lauvaux, T., Davis, K., Miles, N., Richardson, S., and Stauffer, D.: A WRF-Chem Realtime Modeling System for Monitoring CO₂ Emissions, *WRF Users' Workshop 2012*, Boulder, CO, p. 6pp, 2012a.
- Deng, A., Stauffer, D., Gaudet, B., and Hunter, G.: A Rapidly Relocatable High-Resolution WRF System for 725 Military-Defense, Aviation and Wind Energy, *WRF Users' Workshop 2012*, Boulder, CO, p. 11pp, 2012b.
- Deng, A., Lauvaux, T., Gaudet, B., Sarmiento, D., and Davis, K.: Toward Reduced Transport Errors in a High Resolution Urban CO₂ Inversion System, *Elementa*, p. XX, in prep.

- Diaz-Isaac, L. I., Lauvaux, T., Davis, K. J., Miles, N. L., Richardson, S. J., Jacobson, A. R., and Andrews, A. E.: Model-data comparison of MCI field campaign atmospheric CO₂ mole fractions, *Journal of Geophysical Research: Atmospheres*, 119, 10 536–10 551, doi:10.1002/2014JD021593, <http://dx.doi.org/10.1002/2014JD021593>, 2014JD021593, 2014.
- Djuricin, S., Pataki, D. E., and Xu, X.: A comparison of tracer methods for quantifying CO₂ sources in an urban region, *Journal of Geophysical Research: Atmospheres*, 115, n/a–n/a, doi:10.1029/2009JD012236, <http://dx.doi.org/10.1029/2009JD012236>, d11303, 2010.
- Djuricin, S., Xu, X., and Pataki, D. E.: The radiocarbon composition of tree rings as a tracer of local fossil fuel emissions in the Los Angeles basin: 1980–2008, *Journal of Geophysical Research: Atmospheres*, 117, n/a–n/a, doi:10.1029/2011JD017284, <http://dx.doi.org/10.1029/2011JD017284>, d12302, 2012.
- Gaudet, B., Stauffer, D., Seaman, N., Deng, A., Pleim, J., Gilliam, R., Schere, K., and Elleman, R.: Modeling extremely cold stable boundary layers over interior Alaska using a WRF FDDA system, 13th Conference on Mesoscale Processes, Salt Lake City, UT; AMS, p. 9pp, 2009.
- Gerbig, C., Lin, J. C., Wofsy, S. C., Daube, B. C., Andrews, A. E., Stephens, B. B., Bakwin, P. S., and Grainger, C. A.: Toward constraining regional-scale fluxes of CO₂ with atmospheric observations over a continent: 1. Observed spatial variability from airborne platforms, *J. Geophys. Res.*, 108(D24), doi:10.1029/2002JD003 018, 2003.
- Göckede, M., Turner, D. P., Michalak, A. M., Vickers, D., and Law, B. E.: Sensitivity of a subregional scale atmospheric inverse CO₂ modeling framework to boundary conditions, *J. Geophys. Res.*, 115, D24 112, doi:10.1029/2010JD014443, 2010.
- Grell, G., Peckham, S. E., Schmitz, R., McKeen, S. A., Frost, G., Skamarock, W. C., and Eder, B.: Fully coupled online chemistry within the WRF model, *Atmos. Environ.*, 39, 6957–6975, 2005.
- Gurney, K. R.: Recent research quantifying anthropogenic CO₂ emissions at the street scale within the urban domain, *Carbon Management*, 5, 309–320, doi:10.1080/17583004.2014.986849, <http://dx.doi.org/10.1080/17583004.2014.986849>, 2014.
- Gurney, K. R., Mendoza, D., Zhou, Y., Fischer, M., Miller, C., Geethakumar, S., and de le Rue du Can, S.: High resolution fossil fuel combustion CO₂ emission fluxes for the United States, *Environ. Sci. Technol.*, 43(14), 2009.
- Gurney, K. R., Razlivanov, I., Song, Y., Zhou, Y., Benes, B., and Abdul-Massih, M.: Quantification of Fossil Fuel CO₂ Emissions on the Building/Street Scale for a Large U.S. City, *Environmental Science and Technology*, 46, 12 194–12 202, doi:10.1021/es3011282, <http://pubs.acs.org/doi/abs/10.1021/es3011282>, 2012.
- Hutyra, L. R., Duren, R., Gurney, K. R., Grimm, N., Kort, E. A., Larson, E., and Shrestha, G.: Urbanization and the carbon cycle: Current capabilities and research outlook from the natural sciences perspective, *Earth's Future*, 2, 473–495, doi:10.1002/2014EF000255, <http://dx.doi.org/10.1002/2014EF000255>, 2014.
- IPCC, .: Contribution of Working Groups I, II and III to the Fifth Assessment Report of the Intergovernmental Panel on Climate Change, in: *Climate Change 2014: Synthesis Report*, edited by Pachauri, R. and Meyer, L., p. 151, IPCC, Geneva, Switzerland, 2014.
- Kaminski, T., Rayner, P. J., Heimann, M., and Enting, I. G.: On Aggregation Errors in Atmospheric Transport Inversions, *J. Geophys. Res.*, 106, 4703–4715, 2001.

- Karion, A., Sweeney, C., Kort, E. A., Shepson, P. B., Brewer, A., Cambaliza, M., Conley, S. A., Davis, K., Deng, A., Hardesty, M., Herndon, S. C., Lauvaux, T., Lavoie, T., Lyon, D., Newberger, T., Pétron, G., Rella, C., Smith, M., Wolter, S., Yacovitch, T. I., and Tans, P.: Aircraft-Based Estimate of Total Methane Emissions from the Barnett Shale Region, *Environmental Science & Technology*, 49, 8124–8131, doi:10.1021/acs.est.5b00217, <http://dx.doi.org/10.1021/acs.est.5b00217>, 2015.
- Koohkan, M. R. and Bocquet, M.: Accounting for representativeness errors in the inversion of atmospheric constituent emissions: application to the retrieval of regional carbon monoxide fluxes, *Tellus B*, 64, <http://www.tellusb.net/index.php/tellusb/article/view/19047>, 2012.
- Kort, E. A., Frankenberg, C., Miller, C. E., and Oda, T.: Space-based observations of megacity carbon dioxide, *Geophysical Research Letters*, 39, n/a–n/a, doi:10.1029/2012GL052738, <http://dx.doi.org/10.1029/2012GL052738>, 117806, 2012.
- Lauvaux, T., Gioli, B., Sarrazat, C., Rayner, P. J., Ciais, P., Chevallier, F., Noilhan, J., Miglietta, F., Brunet, Y., Ceschia, E., Dolman, H., Elbers, J. A., Gerbig, C., Hutjes, R., Jarosz, N., Legain, D., and Uliasz, M.: Bridging the gap between atmospheric concentrations and local ecosystem measurements, *Geophys. Res. Lett.*, 36, L19809, 5 PP., doi:10.1029/2009GL039574, 2009a.
- Lauvaux, T., Pannekoucke, O., Sarrazat, C., Chevallier, F., Ciais, P., Noilhan, J., and Rayner, P. J.: Structure of the transport uncertainty in mesoscale inversions of CO₂ sources and sinks using ensemble model simulations, *Biogeosciences*, 6, 1089–1102, doi:10.5194/bg-6-1089-2009, <http://www.biogeosciences.net/6/1089/2009/>, 2009b.
- Lauvaux, T., Schuh, A. E., Uliasz, M., Richardson, S., Miles, N., Andrews, A. E., Sweeney, C., Diaz, L. I., Martins, D., Shepson, P. B., and Davis, K. J.: Constraining the CO₂ budget of the corn belt: exploring uncertainties from the assumptions in a mesoscale inverse system, *Atmospheric Chemistry and Physics*, 12, 337–354, doi:10.5194/acp-12-337-2012, <http://www.atmos-chem-phys.net/12/337/2012/>, 2012.
- Lauvaux, T., Miles, N. L., Richardson, S. J., Deng, A., Stauffer, D. R., Davis, K. J., Jacobson, G., Rella, C., Calonder, G.-P., and DeCola, P. L.: Urban Emissions of CO₂ from Davos, Switzerland: The First Real-Time Monitoring System Using an Atmospheric Inversion Technique, *J. Appl. Meteor. Climatol.*, 52, 2654–2668, doi:10.1175/JAMC-D-13-038.1, 2013.
- Marland, G., Rotty, R. M., and Treat, N. L.: CO₂ from fossil fuel burning: Global distribution of emissions, *Tellus*, 37B, 243–258, 1985.
- McKain, K., Wofsy, S. C., Nehrkorn, T., Eluszkiewicz, J., Ehleringer, J. R., and Stephens, B. B.: Assessment of ground-based atmospheric observations for verification of greenhouse gas emissions from an urban region, *Proceedings of the National Academy of Sciences*, 109, 8423–8428, doi:10.1073/pnas.1116645109, <http://www.pnas.org/content/109/22/8423.abstract>, 2012.
- Miles, N. L., Richardson, S. J., Davis, K. J., Lauvaux, T., Deng, A., and Turnbull, J.: Detectability and quantification of atmospheric boundary layer greenhouse gas enhancements from urban emissions: Results from the Indianapolis Flux Experiment (INFLUX), in prep., 1, n/a–n/a, 2015.
- Nisbet, E. and Weiss, R.: Top-Down Versus Bottom-Up, *Science*, 328, 1241–1243, doi:10.1126/science.1189936, <http://www.sciencemag.org/content/328/5983/1241.short>, 2010.
- NRC: Verifying Greenhouse Gas Emissions: Methods to Support International Climate Agreements, The National Academies Press, Washington, DC,

<http://www.nap.edu/catalog/12883/verifying-greenhouse-gas-emissions-methods-to-support-international-climate-agreements>, 2010.

Oda, T.: The Open-source Data Inventory for Anthropogenic CO₂ (ODIAC) emission model version 3.0, Geoscientific Model Development, 2015.

Oda, T. and Maksyutov, S.: A very high-resolution (1km x 1km) global fossil fuel CO₂ emission inventory derived using a point source database and satellite observations of nighttime lights, Atmospheric Chemistry and Physics, 11, 543–556, doi:10.5194/acp-11-543-2011, <http://www.atmos-chem-phys.net/11/543/2011/>, 2011.

Oda, T., Maksyutov, S., and Elvidge, C.: Disaggregation of national fossil fuel CO₂ emissions using a global power plant database and DMSP nightlight data, Proceedings of the Asia-Pacific Advanced Network, 30, 219–228, doi:<http://dx.doi.org/10.7125/APAN.30.24>, 2010.

Ogle, S. M., Davis, K., Lauvaux, T., Schuh, A., Cooley, D., West, T. O., Heath, L. S., Miles, N. L., Richardson, S., Breidt, F. J., Smith, J. E., McCarty, J. L., Gurney, K. R., Tans, P., and Denning, A. S.: An approach for verifying biogenic greenhouse gas emissions inventories with atmospheric CO₂ concentration data, Environmental Research Letters, 10, 034012, <http://stacks.iop.org/1748-9326/10/i=3/a=034012>, 2015.

Richardson, S. J., Miles, N. L., Davis, K. J., Crosson, E. R., Rella, C. W., and Andrews, A. E.: Field Testing of Cavity Ring-Down Spectroscopy Analyzers Measuring Carbon Dioxide and Water Vapor, Journal of Atmospheric and Oceanic Technology, 29, 397–406, doi:10.1175/JTECH-D-11-00063.1, 2011.

Rogers, R. E., Deng, A., Stauffer, D. R., Gaudet, B. J., Jia, Y., Soong, S.-T., and Tanrikulu, S.: Application of the Weather Research and Forecasting Model for Air Quality Modeling in the San Francisco Bay Area, J. Appl. Meteor. Climatol., 52(9), 1953–1973, doi:10.1175/JAMC-D-12-0280.1, 2013.

Saide, P., Bocquet, M., Osses, A., and Gallardo, L.: Constraining surface emissions of air pollutants using inverse modelling: method intercomparison and a new two-step two-scale regularization approach, Tellus B, 63, 360–370, doi:10.1111/j.1600-0889.2011.00529.x, 2011.

Schuh, A. E., Lauvaux, T., West, T. O., Denning, A. S., Davis, K. J., Miles, N., Richardson, S., Uliasz, M., Lokupitiya, E., Cooley, D., Andrews, A., and Ogle, S.: Evaluating atmospheric CO₂ inversions at multiple scales over a highly inventoried agricultural landscape, Global Change Biology, 19, 1424–1439, doi:10.1111/gcb.12141, <http://dx.doi.org/10.1111/gcb.12141>, 2013.

Seibert, P. and Frank, A.: Source-receptor matrix calculation with a Lagrangian particle dispersion model in backward mode, Atmospheric Chemistry and Physics, 4, 51–63, doi:10.5194/acp-4-51-2004, <http://www.atmos-chem-phys.net/4/51/2004/>, 2004.

Skamarock, W. C., Klemp, J. B., Dudhia, J., Gill, D. O., Barker, D. M., Duda, M., Huang, X.-Y., Wang, W., and Powers, J. G.: A Description of the Advanced Research WRF Version 3, National Center of Atmospheric Research, Tech. Note, NCAR/TN-475+STR, 113pp, 2008.

Stauffer, D. and Seaman, N.: Multiscale Four-Dimensional Data Assimilation, J. Appl. Meteor., 33, 416–434, 1994.

Tarantola, A.: Inverse Problem Theory and Methods for Model Parameter Estimation, SIAM, (ISBN 0-89871-572-5), 2004.

Thomson, D. J.: Criteria for the selection of stochastic models of particle trajectories in turbulent flow, J. Fluid Mech., 180, 529–556, 1987.

- Turnbull, J. C., Karion, A., Fischer, M. L., Faloona, I., Guilderson, T., Lehman, S. J., Miller, B. R., Miller, J. B., Montzka, S., Sherwood, T., Saripalli, S., Sweeney, C., and Tans, P. P.: Assessment of fossil fuel carbon dioxide and other anthropogenic trace gas emissions from airborne measurements over Sacramento, California in spring 2009, *Atmospheric Chemistry and Physics*, 11, 705–721, doi:10.5194/acp-11-705-2011, <http://www.atmos-chem-phys.net/11/705/2011/>, 2011.
- Turnbull, J. C., Sweeney, C., Karion, A., Newberger, T., Lehman, S. J., Tans, P. P., Davis, K. J., Lauvaux, T., Miles, N. L., Richardson, S. J., Cambaliza, M. O., Shepson, P. B., Gurney, K., Patarasuk, R., and Razli-
vanov, I.: Toward quantification and source sector identification of fossil fuel CO₂ emissions from an urban
area: Results from the INFLUX experiment, *Journal of Geophysical Research: Atmospheres*, 120, 292–312,
doi:10.1002/2014JD022555, <http://dx.doi.org/10.1002/2014JD022555>, 2015.
- Uliasz, M.: Lagrangian particle modeling in mesoscale applications, in: *Environmental Modelling II*, edited by
Zanetti, P., Computational Mechanics Publications, pp. 71–102, 1994.
- United Nations, D. o. E. and Social Affairs, P. D.: *World Urbanization Prospects: The 2014 Revision, Highlights*,
United Nations (ST/ESA/SER.A/352), 2014.
- Wu, L., Bocquet, M., Chevallier, F., Lauvaux, T., and Davis, K.: Hyperparameter estimation for uncertainty quantification in mesoscale carbon dioxide inversions, *Tellus B*, 65,
<http://www.tellusb.net/index.php/tellusb/article/view/20894>, 2013.